Effects of Environmental Temperature and Humidity on the Geometry and Strength of Polycarbonate Specimens Prepared by Fused Filament Fabrication[1]

Lichen Fang [1], Yishu Yan [1], Ojaswi Agarwal [1], Shengyu Yao [1], Jonathan E. Seppala [2,*] and Sung Hoon Kang [1,*]

[1] Department of Mechanical Engineering and Hopkins Extreme Materials Institute, Johns Hopkins University, Baltimore, MD 21218, USA;
[2] Materials Science and Engineering Division, National Institute of Standards and Technology, Gaithersburg, MD 20899, USA;
* Correspondence: jonathan.seppala@nist.gov (J. E. Seppala), shkang@jhu.edu (S. H. Kang)

Abstract: It is widely known that the printing quality of fused filament fabrication (FFF) is heavily affected by environmental temperature and humidity, as the case of warping and porosity. However, there is little understanding about the quantitative relations between environmental conditions and geometry and mechanical properties of printed parts. In this study, we have systematically investigated those relations using bisphenol A polycarbonate as a model material system. For the environmental temperature, in-situ infrared imaging analysis revealed the presence of up to 5.4 °C/mm thermal gradient when printing using an open-chamber printer and a heated build plate. For the environmental humidity, analysis of X-ray micro-computed tomography (micro-CT) scans showed up to 11.7 % porosity, which is brought by polymer water content absorbed from environmental moisture. Meanwhile, tensile tests showed the mechanical performance loss associated with those defects, but surprisingly the transverse direction ductility may increase at higher porosity. Furthermore, the experimental results are combined with analytical and parametrical studies to elucidate quantitative relations between environmental conditions and printing quality. Based on the results, quantitative guidelines for estimation of printing quality based on environmental conditions are provided, which would also help users to obtain desired printing results with a better understanding of the effects of environmental conditions.

Keywords: fused filament fabrication; environmental temperature; humidity; X-ray micro-computed tomography; porosity; mechanical properties.

1. Introduction

Fused filament fabrication (FFF)[2] is one of the most popular additive manufacturing methods. It allows users with minimum training to easily convert their digital designs into real items at low cost. Hence, it is widely applied in highly customized parts and prototyping [1]. However, compared to other fabrication methods, the relatively inferior mechanical properties and commonly appearing printing defects limit FFF for more applications in industrialized productions [2,3]. To overcome this issue, scientists and engineers have been devoted to improving the FFF process and printing quality via optimizing printing parameters [4,5,6]. Nevertheless, the environmental factors such as chamber/build plate temperature and humidity [7], have long been insufficiently studied even though it was reported that they could significantly impact the printing quality: including introducing geometrical defects like warping and porosity, and reducing mechanical performance like strength [8,9].

To mitigate temperature-induced defects, a low cost and straightforward solution is adding a heated build plate to keep the specimen warm during printing. However, it was shown that a heated build plate could not provide a uniform temperature field across the entire building area, so that there still existed thermal-induced defects [10]. Then, the more expensive while effective solution is controlling the temperature of the printing chamber, and there have been multiple numerical studies focusing on its effects on melt polymer flow [11], interfacial bonding [12], heat transfer [13], specimen distortion [14,15], etc. However, since most open-source FFF printers do not have temperature-controlled chambers, there are much fewer experimental efforts reported. Sun, *et al.* built a chamber

[1] Official contribution of the National Institute of Standards and Technology; not subject to copyright in the United States.

[2] Material Extrusion is the ASTM/ISO defined term for Fused filament fabrication (FFF), however, FFF is used more commonly in the literature. The process described as fused deposition modeling (FDM) is a trademark of Stratasys, Inc.

for printing PEEK, which requires a high environmental temperature to print, and they found a significant improvement in specimen strength [16]. Spoerk, *et al.* printed polypropylene filled with glass spheres, which showed better annealing quality and dimensional accuracy with elevated chamber temperature [17,18]. Carneiro, *et al.* found a 20 °C increase in environmental temperature reduced the structural porosity of printed ABS by 50 % [19]. Armillotta, *et al.* studied the specimen warpage with both analytical and experimental approaches and reported a high chamber temperature close to glass transition temperature significantly reduced the warpage [20].

Environmental humidity is another primary source of printing defects in FFF, though it is highly varied from material to material, considering the different water absorption properties of various polymers[21]. For the polycarbonate (PC) that we are interested in, there have been some water absorption studies decades ago, investigating the physical property changes [22] and influence to the injection molding applications [23]. Ito *et al.* found PC could absorb up to 0.2 % by mass of water within 3 h under 24.5 °C and 88 % relative humidity (RH) [24]. Multiple studies have demonstrated that the mechanical properties of PC are reduced upon water absorption. The primary mechanism behind this property reduction is attributed to microstructural defects as the absorbed water clusters can lead to the formation of microcracks [23,25,26].

However, the water absorption is closely related to the material geometry (cylindrical filaments in our case), and the FFF process is also different from injection molding considering the heating time, material quantity, and seal of the mold. Thus, a study specifically designed for FFF is required. There have been very few papers published in this area. Halidi, *et al.* have studied the moisture sorption effects on ABS filaments and confirmed it would not cause nozzle clogging [27]. Kim, *et al.* studied the water absorption of printed ABS specimens and their corresponding property changes. The humidity was introduced together with a higher temperature, showing the printed parts have significant aging effects, and the strength is reduced when storing in hot and humid conditions [28]. Valerga, *et al.* studied the effects of humidity on PLA printing and they found the material could degrade during storage and create bubbles when printing, hence reducing the mechanical strength of printed parts [29].

Overall, researchers have noticed the negative effects brought by environmental conditions, but more thorough and systematic studies are needed to quantitatively understand those influences on the printing process. In this paper, we investigate those issues step by step. For temperature effects, we first measure the temperature field using an infrared camera and obtain the thermal gradients within specimens printed under different environmental temperatures. Then, from the thermal gradients, we predict the warpages and compare with experimental measurements. Finally, we perform tests to capture the mechanical property changes. For humidity effects, we start with a water absorption test to quantify how much water printed materials can absorb under different levels of humidity. With the water content, we estimate the corresponding porosity, which was compared with experimental results obtained from micro-CT scans. Eventually, uniaxial tensile test results were analyzed together with pore size data to under processing-microstructure-property relations.

2. Materials and Methods

2.1. Fabrication

A LulzBot TAZ 6 printer[3] with 0.5 mm nozzle diameter was used as the main equipment for fabrication, around which a low-cost environmental control system was built. As **Figure 1(a)** shows, the printer is enclosed with an acrylic chamber (Printed Solid, Inc.). A hole was cut on the top surface to connect to compressed dry air, which is pumped in during printing to keep the environmental humidity below 10 % RH. A space heater (STEGO, Inc.) was mounted inside the chamber and connected to a temperature controller, which can vary the environmental temperature from room temperature (20 °C) to 90 °C. For the filament feedstock, bisphenol-A-polycarbonate was used as the model material system. The original mechanical properties of the 2.85 mm Ultimaker PC filaments were measured for comparison (see Figure S1 and Table S1 for details). To keep the initial conditions constant, all filaments were dried

[3] Certain commercial equipment, instruments, or materials are identified in this paper in order to specify the experimental procedure adequately. Such identification is not intended to imply recommendation or endorsement by the National Institute of Standards and Technology, nor is it intended to imply that the materials or equipment identified are necessarily the best available for the purpose.

for 1 h in a vacuum oven set at 100 °C. Meanwhile, PC's zero-shear viscosity was obtained by performing a 120 °C - 280 °C temperature sweep measurement using Anton-Paar MCR 302 rheometer.

To study the effects of varying environmental conditions, temperature and humidity were varied separately, i.e., the environmental humidity was kept below 10 % RH when studying temperature effects, and the temperature was set at 22 °C when studying humidity effects. Afterward, the corresponding physical and mechanical effects were also investigated. For environmental temperature, four different values (30 °C, 50 °C, 70 °C, 90 °C) were tested: the entire chamber was heated and kept around a target temperature during the printing process. The temperature fluctuation was around ± 5 °C, since the acrylic chamber has limited thermal insulation. For the effects of PC water absorption under different levels of humidity, a lab balance attached with a Cellkraft P-2 humidifier was used (see Figure S2(a) for details). The environmental humidity could be controlled with ± 1 % RH fluctuation. Dried PC filaments were then exposed to four different humidity levels (10 % RH, 30 % RH, 50 % RH, 70 % RH) for 24 h to study the water absorption rate, and the resulting filaments with different water contents (0 % by mass, 0.05 % by mass, 0.1 % by mass, 0.15 % by mass) were printed and tested. Despite the varied environmental conditions, all other printing parameters were kept same, including layer height (0.3 mm), nozzle temperature (280 °C), print speed (10 mm/s), and build plate temperature (115 °C).

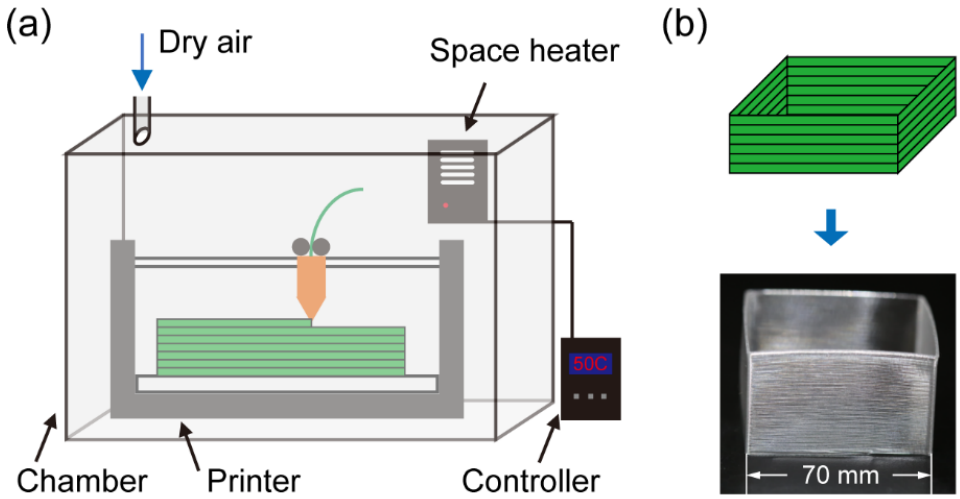

Figure 1. (**a**) Schematic of the printer and the environmental control system; (**b**) The illustration and picture of the printed hollow box geometry.

The bonding between two stacked fiber tracks is a critical part that determines the properties of the FFF printed parts. To study how the bonding property changes with environmental conditions, we created a 70 mm by 70 mm by 50 mm hollow box geometry, as **Figure. 1(b)** shows. Each side of the box is a single-track wide wall, made with multiple tracks printing one over another. The width of the wall was set to be equal to the nozzle diameter of 0.5 mm. After fabrication, the specimens were cut to smaller pieces for either micro-CT scan or mechanical tensile tests.

2.2. Characterizations

Three characterization techniques were applied to measure the property changes upon varying environmental conditions. First, for the temperature side, infrared (IR) thermography was used to evaluate the temperature field of the specimen during printing. As **Figure 2(a)** shows, an IR camera (FLIR a6701sc camera with 50 mm F/2.5 lens) was mounted facing a round opening in the front panel of the printer chamber. The opening was drilled to allow infrared light transmission, since acrylic is not transparent to infrared. Calibration of the PC emission spectrum was performed, as shown in Figure S3 [30]. The measured photon counts were later imported into MATLAB for conversion to the temperature field and performing further analysis. During printing, we found the extruded material temperature could

be 15 °C lower than the nozzle temperature set at 280 °C. However, IR thermography could not measure the material temperature when it is inside the nozzle, and the material cools down rapidly after leaving the nozzle. Thus, the real material temperature could be between 265 °C and 280 °C. After printing, pictures of the specimens were taken using a Canon EOS 80d DSLR with 100 mm F/2.8 USM macro lens. The images have resolutions of 15 μm/pixel and were later used to quantify the warping deformation associated with thermal gradient.

To gain more understanding on the humidity effect, the as-printed specimens were scanned by Bruker Skyscan 1172 micro-CT with 4.87 μm resolution. All pores larger than 10 μm could be identified and segregated (smaller pores cannot be detected), using the post-processing software package Dragonfly. As **Figure 2(b)** shows, each pore was labeled separately using the watershed transformation algorithm, and then statistics of the pore size distribution and overall porosity could be obtained.

Finally, tensile tests were conducted on all printed specimens using Instron E1000 mechanical testing system. Following the ASTM D1708 standard, the specimens were laser cut into dogbone geometry with 12 mm by 5 mm gauge area, as **Figure 2(c)** shows. The tests were performed quasi-statically, with 0.01 mm/s testing speed. The specimens were tested both along and perpendicular to the printing direction to investigate the anisotropy. The resulting force-displacement curves were then normalized to stress-strain curves for more general comparisons. The strain was measured by optical monitoring (see Figure S4 for details), and the stress was calculated via forces divided by CT-measured average cross-section areas (see Figure S5 for details).

To confirm the statistical significancy, all warping deflections and mechanical testing results were examined with analysis of variance (ANOVA) using the MATLAB statistics toolbox. This analysis can compare the mean values between groups of samples and determine whether they have the same mean values.

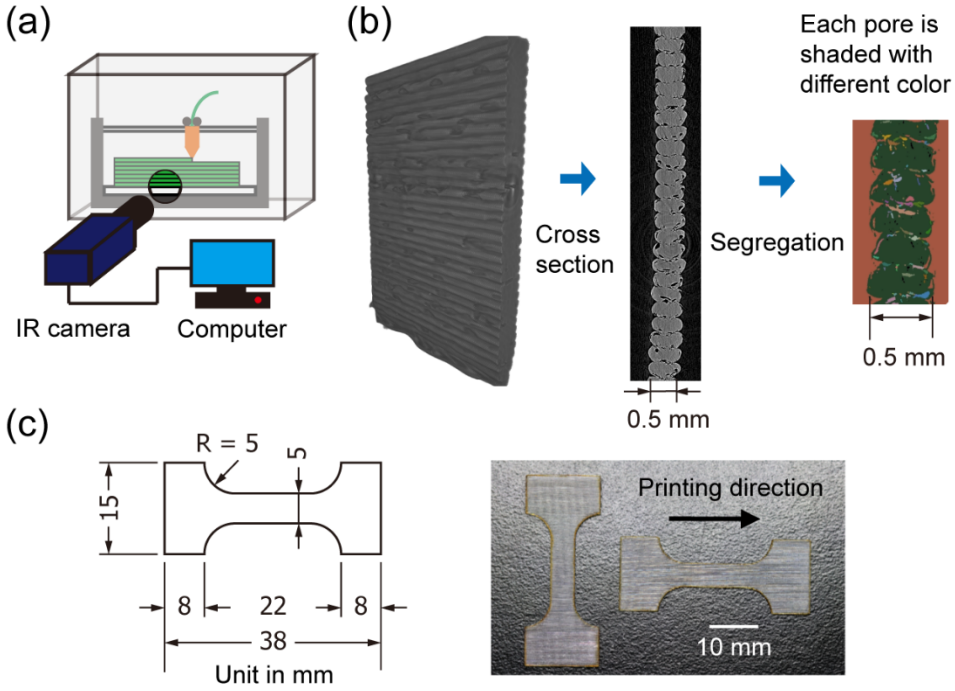

Figure 2. (**a**) Schematic of the infrared thermography system; (**b**) Illustration of the void segregation of scanned specimens; (**c**) Drawing and pictures of the dogbone tensile specimens.

3. Results and Discussions

3.1. Effects of varying environmental temperature

In this subsection, the relations among environmental temperature, specimen thermal gradient, warping defects, and mechanical properties were investigated and discussed. An analytical estimation of the warping deformation was also proposed and examined.

3.1.1. Characterizations of temperature fields within specimens

Using the infrared camera, the pseudo-color thermography images of four specimens were plotted and labeled in **Figure 3(a)**, representing the thermal profiles right after printing under four different environmental temperatures. Within the pictures, the bottom part is the build plate, which has a constant temperature; the top part is the far-side acrylic chamber background (out of focus), which represents the rising environmental temperature; in the middle is the specimen being printed, which has a clear layer-by-layer structure. To be noted here, the bright and dark strips in specimens do not indicate there are quite different temperatures. They are mostly due to the differences in the surface normal: if the surface is facing the camera, the sensor receives maximum radiation and has the correct temperature reading; otherwise at the connecting point between two layers, the surface normal is not pointing toward the lens, and the infrared emission received by the lens is smaller so the temperature reading is lower. Due to similar reasons, we also see the build plate has a lower temperature reading than its set value.

In the images, it is obvious that the thermal gradient from bottom to top of the specimen has changed significantly with the change in the environmental temperature. The temperature gradients were quantified and plotted in **Figure 3(b)**, from which we could see the specimen temperature decreasing with the distance from the build plate. At 30 °C, a 5.4 °C/mm thermal gradient was observed; while the thermal gradient was reduced to 2.7 °C/mm when the environmental temperature increased to 90 °C.

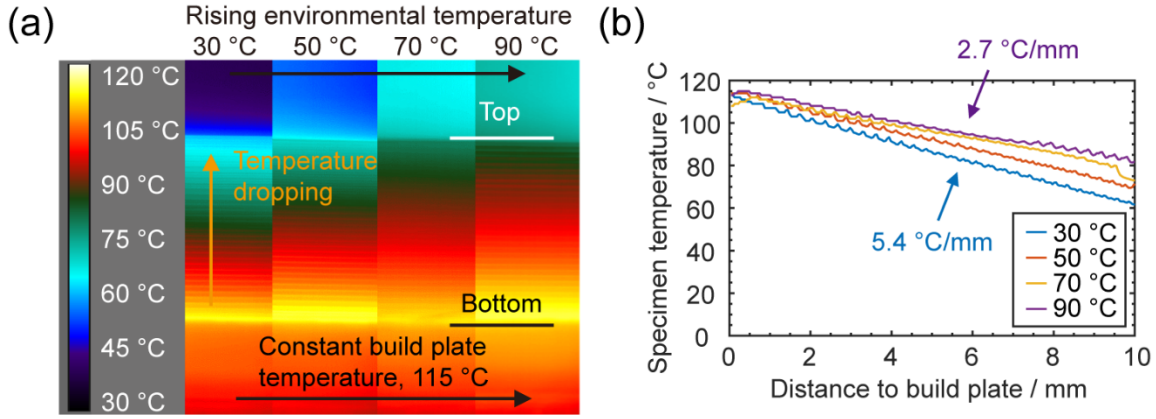

Figure 3. (**a**) Infrared images of specimens being printed under different environmental temperatures; (**b**) The plot of specimen temperatures at different heights.

3.1.2. Warping defect predictions and measurements

With the thermal gradient, strain mismatches were brought by the different thermal expansions in different layers, causing warping defects. From polymer theory, PC is highly viscous before cooling down to glass transition temperature (see Figure S6 for measurements); after passing that point, any further thermal shrinkage will create corresponding elastic thermal stress [20]. From previous literature, we can consider only elastic and plastic deformations in PC's glassy state, while the viscosity is extremely high (> 10^{21} MPa·s at room temperature) [31]. At higher layers, which are cooler, there is a larger temperature difference between specimen temperature and glass transition temperature, so that PC shrinks more than in the lower and warmer layers. As a result, the entire printed specimen tends to bend upward. This deflection is mitigated with a higher environmental temperature, which generates a smaller thermal gradient, as **Figure 4(a)** shows.

Given the observed thermal gradient, it is possible to analytically predict the corresponding warpage. In our case, the maximum thermal strain is smaller than 2 %, which is within the linear region of the stress-strain curve (Figure S1), so that no plasticity is involved. For a slender beam without external constraint, the warping-induced curvature could be estimated as:

$$\kappa = \alpha(T)\frac{(T_g - T_{top}) - (T_g - T_{bottom})}{H} = \alpha(T)\frac{dT}{dz}, \quad (1)$$

here α(T) is the coefficient of thermal expansion (see Figure S7 for measurements), L is the beam length (considering the symmetry, we use 35 mm here), H is the beam height; T_g is the glass transition temperature; T_{top} and T_{bottom} are the temperatures at top and bottom of the specimen. The temperature/height term is equal to the thermal gradient along height/Z direction, marked as dT/dz, the measured values have already been given in **section 3.1.1**.

However, since our specimen is not a slender beam, the shear deformation cannot be ignored. Hence, we applied a correction based on Timoshenko beam theory as Eq. (2) [32,33]:

$$\kappa_T = (1 + \frac{2EI}{KL^2AG})\alpha(T)\frac{dT}{dz}\ , \tag{2}$$

where E is the elastic modulus, G is the shear modulus (E/G = 2.7 for PC), I is the second moment of area, A is the cross-section area, K is the Timoshenko shear coefficient (equals to 5/6 for a rectangular section).

To evaluate the model, we compared the calculated curvatures with experimental measurements, as shown in **Figure 4(b)**. From ANOVA analysis, the p-value is 2.16 E-4 indicating that the average curvature for each group is significantly different. The model can also capture this warping curvature decrease upon an increasing environmental temperature. The discrepancy, especially for the overestimation at 90 °C, could be attributed to the adhesion effects. The adhesion force between the build plate and the specimen could compensate for the bending moment induced by thermal stress, especially at higher temperatures when the thermal stress is smaller. Here in experiments, we tried to minimize the adhesion effects to fulfill the 'no external constraint' condition in our model. While in practice, the adhesion force could depend on multiple factors including material pair, build plate temperature, glues, first layer geometry, etc.

From this mechanism, there could be two ways to reduce thermal deflection. The first one is increasing the adhesion force between the build plate and printed specimen. However, a concern here is the thermal stress still exists during printing. And if it is large enough, it may overcome the bonding force between layers and cause delamination. The second option is increasing the environmental temperature, from our observation, it continuously mitigates the warping defects.

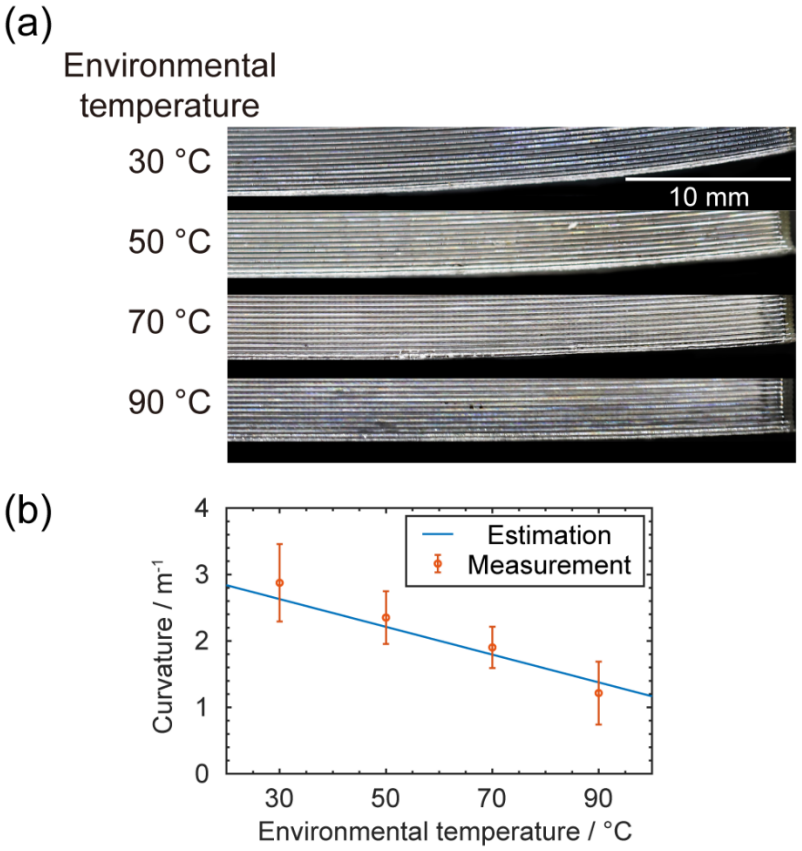

Figure 4. (**a**) Pictures of specimens with warping deflections; (**b**) The plot of predicted deflections and measurements of deflections with respect to the changing environmental temperatures. The error bars are from standard deviations of data obtained from five measurements.

3.1.3. Impacts on mechanical properties

Finally, the mechanical strengths of printed specimens were measured, and the stress-strain curves were plotted. For the longitudinal direction (stretching along the printing direction), the ductile mechanical responses are similar to those of bulk PC, as **Figure 5(a)** shows. In **Figure 5(b)**, the ultimate tensile strengths also show a slightly increasing trend with increasing environmental temperature, from ANOVA analysis the p-value is 0.0240, indicating it is not a significant change. This increasing trend could be due to the mitigation of geometrical defects, including warping and delamination. With less warping, the extrudates are better aligned to the testing direction, which provides higher strength. Eventually, by printing at 90 °C, the strength could approach that of the bulk material.

For the transverse direction (stretching perpendicular to the printing direction), the mechanical performance is significantly reduced, and exhibits brittle behavior, suggesting a strong anisotropy, as **Figure 5(c)** shows. The earlier fracture of specimens is primarily attributed to the non-uniform cross-section geometry in the transverse direction; the bond between two layers is always narrower, and hence easier to break. Thus, environmental temperatures play less important role here. Comparing different environmental temperatures, the p-value of strength in transverse direction is 0.273, suggesting the change is not statistically significant, as **Figure 5(d)**.

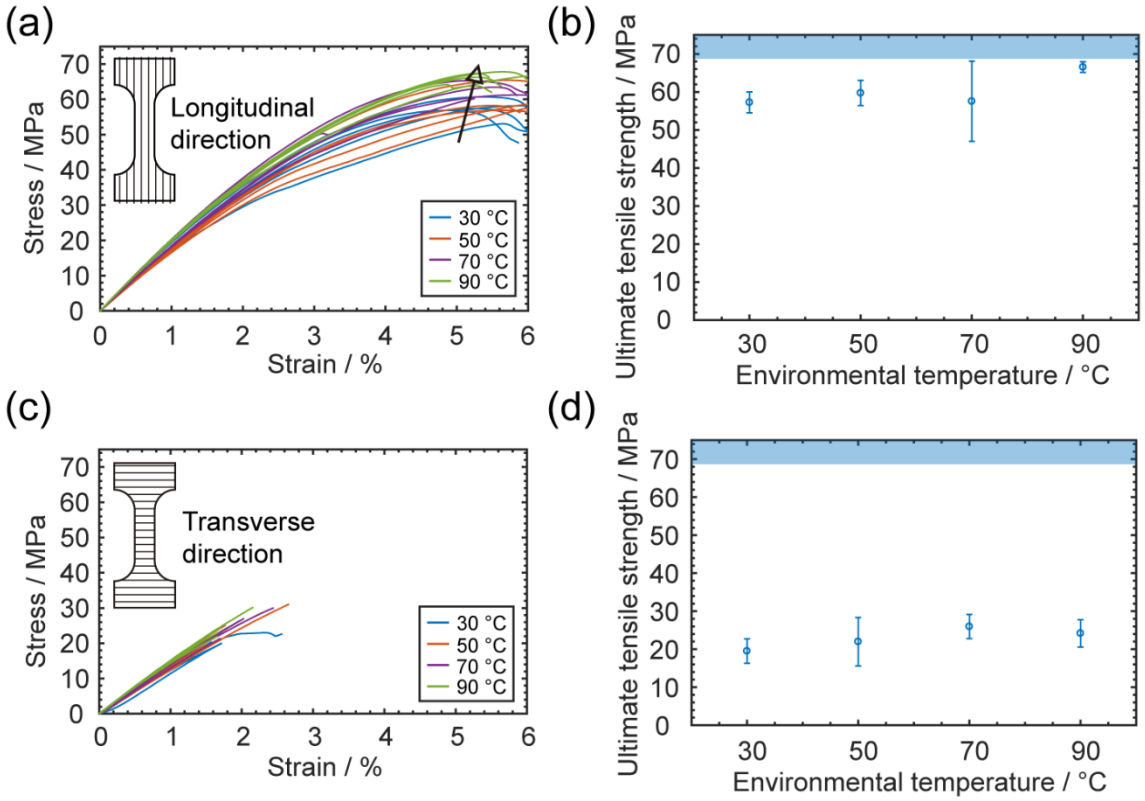

Figure 5. Mechanical effects of varying environmental temperature. (**a**) Stress-strain curves of tensile specimens tested longitudinally; (**b**) Ultimate tensile strengths of longitudinal specimens printed with different environmental temperatures. The reference value of unprinted bulk PC is denoted as the pale blue shaded region; (**c**) Stress-strain curves of tensile specimens tested transversely; (**d**) Ultimate tensile strengths of transverse specimens printed with different environmental temperatures, the error bars are from standard deviations of data obtained from five measurements. The reference value of unprinted bulk PC is denoted as the pale blue shaded region.

3.2. Effects of varying environmental humidity

In this subsection, the relationship between environmental humidity, specimen porosity, and mechanical properties was investigated and discussed. An analytical estimation of the porosity was also proposed and examined.

3.2.1. Water absorption of PC

To investigate the effects of environmental humidity, the first task is to understand how much water the PC could absorb. As described in **section 2.1**, the mass change of 20 g of dried PC filaments had been monitored for 24 h with exposure to five different humidity levels, ranging from 10 % RH to 90 % RH with 20 % RH increment. After experiments, the filaments were re-dried and measured to make sure they return to the original mass, to confirm the mass change is purely due to moisture absorption. The results were plotted in **Figure 6**, except for the results under 90 % RH, in which we observed significant droplet condensation and mist in the lab balance chamber (see Figure S2(b) for details), so that measurement was discarded.

All four curves showed very high water absorption rate at the beginning, and the rate gradually dropped with time, until the curve reached a plateau. The measured saturation points were around 0.01 % by mass, 0.05 % by mass, 0.10 % by mass, and 0.15 % by mass, respectively. The results are comparable with previously reported data [24]. When those filaments are printed, the stored water evaporates due to the heat and creates undesirable pores within specimens. According to previous literature, the water diffusion depth in cylindrical filaments is proportional to the square root of time multiplied by diffusivity [34]. Thus, the interior core and exterior surface of the filaments may have different water contents and result in different porosities and mechanical properties.

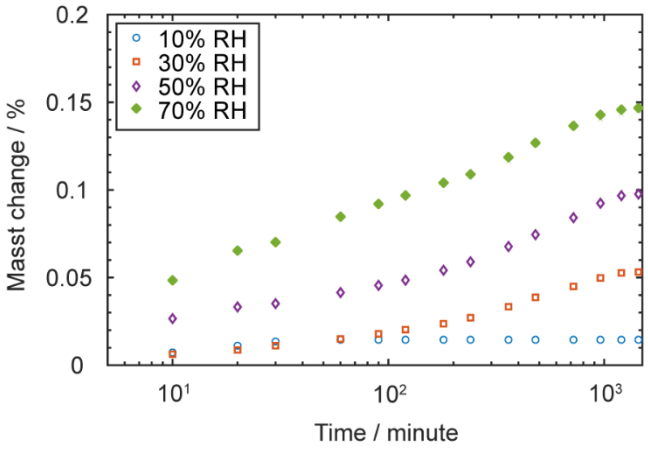

Figure 6. The mass change over time of PC filaments exposed to different humidity levels, specimens saturated after 24 h.

3.2.2. Characterizations of pore defects

We obtained several specimens by printing the filaments with different water contents. To characterize their porosity, micro-CT scans were conducted. Four representative scanned cross-sections of the specimens are plotted in **Figure 7(a)**. For printing with dried filament, the porosity is as low as 0.16 % by volume, while for high water content filament (0.15 % by mass), the printed specimen has porosity up to 11.7 % by volume, and the overall geometry is highly non-uniform.

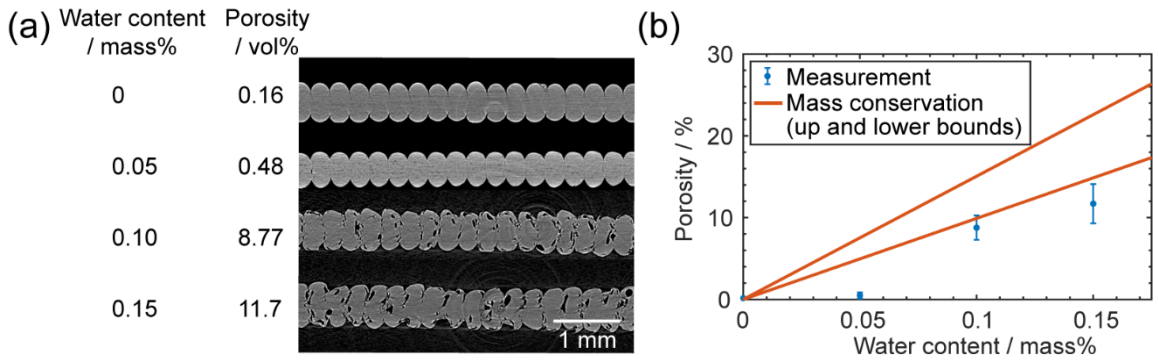

Figure 7. (**a**) The CT-scanned cross sections of printed specimens using filaments with different water contents; (**b**) The comparison between measured porosity and predicted porosity using mass conservation.

If we assume that all the water is vaporized and hence creates pores inside the specimen, we could calculate the corresponding vapor volume from mass conservation. Similar to other gases, water vapor is not an ideal gas, and corrections need to be applied to the ideal gas law as Eq. (3) [35]:

$$\frac{P}{\rho RT} = 1 + B\rho + C\rho^2 + \cdots \tag{3}$$

where P is the pressure inside the nozzle; ρ is the molar density, which is correlated with both vapor mass and volume; R is the gas constant of 8.314 J/(K·mol); T is the material temperature, which in principle shall be equal to the nozzle temperature of 280 °C (553 K), but in practice it could be lower considering thermal conduction takes time [36]. From our IR observation, the material temperature could be 15 °C lower than nozzle temperature after coming out of the nozzle. This shall serve as the lower bound of the material temperature since IR thermography could not measure the temperature inside the nozzle, and the material cools down rapidly in ambient environments. Thus, we made another calculation based on the temperature of 265 °C (538 K). Finally, B and C in **Eq. (3)** are the Virial coefficients that are characterizing the interaction potential between particles (B for two particles, C for three, etc.), which provide systematic corrections to the ideal gas law. In practice, the higher-order Virial coefficients (C and beyond) are often ignored since interactions between three and more molecules are less likely to happen in the gas phase [37]. While the water vapor's second Virial coefficient B has been extensively studied and could be estimated by a fitted equation as Eq. (4) [38]:

$$\frac{B(T)}{B^0} = \sum_{i=1}^{4} a_i * (T^*)^{b_i} \tag{4}$$

where B_0 is 1000 cm^3/mol, T^* is T/100K, a_1 is 0.34404, b_1 is -0.5, a_2 is -0.75826, b_2 is -0.8, a_3 is -24.219, b_3 is -3.35, a_4 is -3978.2, b_4 is -8.338. And the calculated B at 553 K is -128.17 cm^3/mol, while at 538 K is -138.73 cm^3/mol.

The final unknown parameter is the internal pressure, which is hard to measure. A previous literature has reported an estimation approach derived from the Navier-Stokes equation as Eq. (5) [39]:

$$P_{nozzle\_approx} = \frac{12\mu qD}{h_l^3} - \frac{6\mu v_p D}{h_l^2} \tag{5}$$

here the viscosity μ is measured to be 249.88 Pa·s for our PC under 280 °C and 354.83 Pa·s under 265 °C, using Anton-Paar MCR 302 rheometer; q is the volumetric flow rate normalized by a unit length in the Y direction, which is 36.67 mm^2/s for our printing parameters; D is the nozzle diameter of 0.5 mm, v_p is the print speed of 10 mm/s, h_l is the layer height of 0.3 mm. Finally, the pressure is estimated to be 1.95 MPa at 280 °C and 2.77 MPa at 265 °C.

From **Eqs. (3) - (5)**, we calculate the water vapor's molar density (ρ) to be 450.10 mol/m^3 at 280 °C and 684.23 mol/m^3 at 265 °C. Then, the porosity is estimated as:

$$\text{Porosity} = \text{water content} * \rho_{PC}/\rho M_{water} \tag{6}$$

where the density of PC is 1.22 g/cm^3, M_{water} is the molar mass of water as 18 g/mol. Substituting different water contents into **Eq. (6)** we could get the estimation of the porosity. The comparison between this mass-conservation model and measured values is plotted in **Figure 7(b)**, from which we could find the model's values are significantly higher than measured values. This could be due to two primary reasons; the first one is the water vapor may escape from the specimens, especially for water distributed near the exterior surfaces of the filaments; the second reason is the limitation of our measurement capability: our micro-CT scans ran at 4.87 μm/pixel, meaning all the pores smaller than that threshold remained undetected, however, they could contribute to the overall porosity.

To further quantify the size distribution of those pores, the Dragonfly software package was used to segregate each pore and statistically analyze the pore size distribution. The results are shown in **Figure 8**, which illustrates the empirical Cumulative Distribution Function (CDF) [40] for the pore sizes. We find that higher water content leads to higher percentages of large pores, and, the volume of the largest pores also increases with the water content. As a result, according to fracture mechanics, samples with the larger pores should have a lower mechanical strength as the pores serve as initiation sites and help propagate cracks.

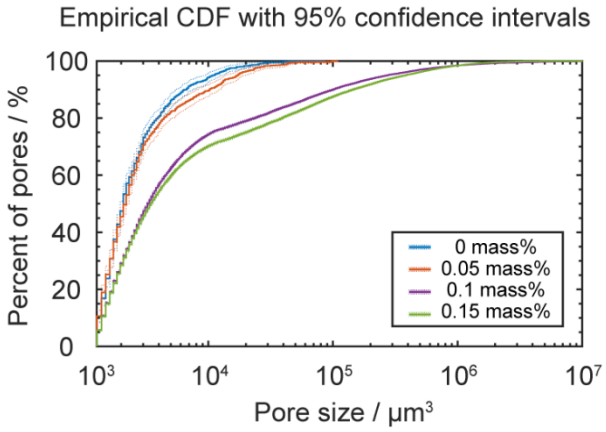

Figure 8. Empirical cumulative distribution functions (CDF) for the pore sizes of printed specimens using filaments with different water contents, dotted lines indicate the upper and lower bounds of 95% confidence intervals.

3.2.3. Impacts on mechanical properties

Finally, we investigated the mechanical performance changes with pore defects. Previous literature showed that the injection-molded PC's mechanical properties dropped upon water absorption, mainly due to two reasons: one is the absorbed water clusters can lead to the formation of microcracks [23,25,26]; the other is the molecular weight reduction upon hydrolysis [41]. For our case, the printed materials have been extruded from the hot nozzle and then kept on the 115 °C build plate for hours, so that the specimen is expected to have minimal water content after printing. This was further confirmed by additional drying experiments in which the printed specimens are measured to have the same mass before and after drying. Even without any water content, the pore defects remaining inside the specimen from the water absorbed by the filament can still impact the mechanical properties, this shall be accounted as a geometrical factor and will be discussed below. For the hydrolysis reaction, it is a much slower process that takes months to show a significant difference [41], thus it does not need to be accounted for in this study.

For the longitudinal direction (stretching along the printing direction), the mechanical behavior is still ductile, as **Figure 9(a)** shows. However, there is a significant loss in ultimate tensile strength when printing with higher water content (p-value is 6.91 E-5 under ANOVA analysis). As **Figure 9(b)** shows, the strength decreases around 30 % compared to printing with dry filament, for which the strength is close to that of a bulk PC. This loss can be attributed to the porosity. The randomly distributed pores reduce the effective area of the cross-section as well as create a stress concentration, which greatly weakens the specimens.

For the transverse direction (elongated perpendicular to the printing direction), again the mechanical performance is reduced, and the deformation behavior becomes brittle, meaning the ultimate tensile strength is also the fracture strength, as **Figure 9(c)** shows. Here we observed a very interesting trend of mechanical property change (p-value is 5.26 E-10): both fracture strength and strain initially decreased but later increased with the increase in water content, as shown in **Figure 9(d)**. This phenomenon only happens in the transverse direction, suggesting it could be a combined effect of the printed geometry and pore defects. As the illustrations in **Figure 10(a)** show, when there is no porosity, the weld point between two layers could initiate the crack, and the crack propagates along the relatively narrow bond; when some porosity is introduced, the extra pores could help the crack initiation and propagation, leading to a lower fracture strength; however, when the porosity is high, the randomly distributed pores may deviate the crack and let it propagate along a longer path, which might introduce some extra ductility to the specimens. Evidence for this hypothesis is the pictures shown in **Figure 10(b)**, from which we could see for no water content, the crack is exactly along the bond between two layers; while for higher water content, the crack deviates from the bond and propagates across multiple layers.

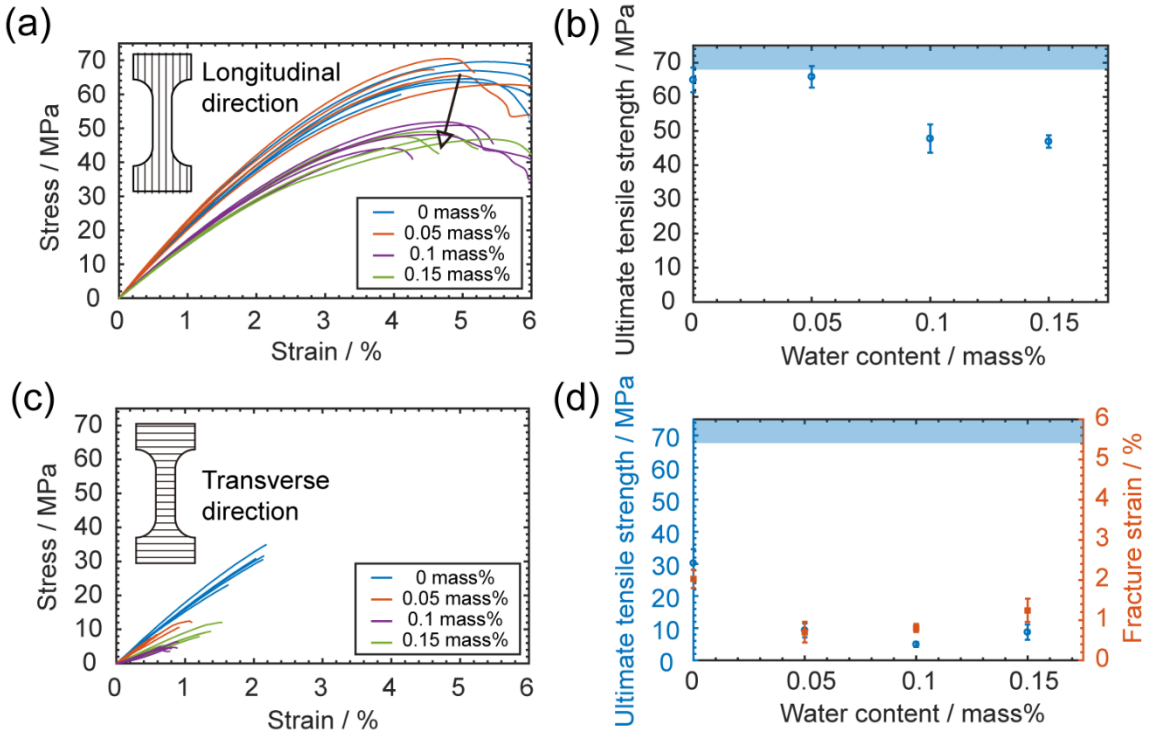

Figure 9. Mechanical effects of varying water content. (**a**) Stress-strain curves of tensile specimens tested longitudinally, arrow indicates the dropping strength with higher water content; (**b**) Ultimate tensile strengths of longitudinal specimens printed with different water content, the reference value of unprinted bulk PC is denoted as pale blue shaded region; (**c**) Stress-strain curves of tensile specimens tested transversely; (**d**) Ultimate tensile strengths and fracture strains of transverse specimens printed with different water content. The error bars are from standard deviations of data obtained from five measurements. The reference value of unprinted bulk PC is denoted as pale blue shaded region.

As a summary, the porosity brought by moisture absorption could significantly impact both the geometry and mechanical performances of printed specimens. The pores not only make the product rougher, but also decrease the uniformity of the printing pattern. For the mechanical side, the strengths will decrease in both the longitudinal and transverse directions with water content. Though some extra ductility could be introduced at very high water content, the mechanical performance is still worse than that of printing with dried filaments.

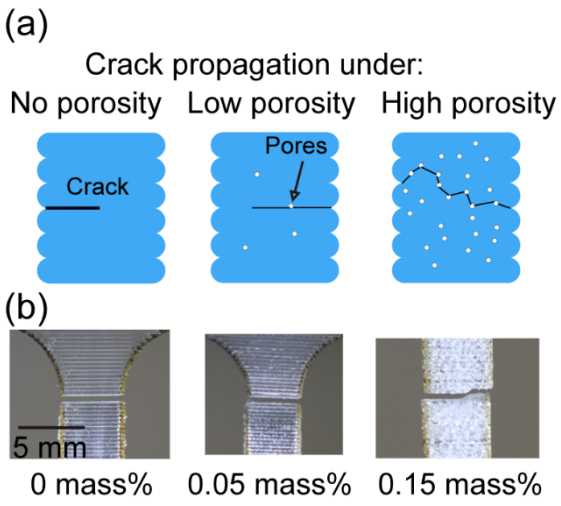

Figure 10. (**a**) Illustrations of crack formations with different porosities. (**b**) Images of cracks.

Combining the mechanical tests with the water absorption test results shown in **section 3.2.1**, to avoid water in the print, it is not sufficient to only dry filaments beforehand, but also is important to minimize the moisture absorption during printing. The absorption rate of water into PC is very fast at the beginning. For example, if less than 0.05 % by mass water content is desired, printing could either be performed under 30 % RH with dry filaments-- as long as the printing does not take a full day; otherwise a dry environment is also required since PC can absorb 0.05 % by mass of water in less than 2 h at > 50 %RH humidity.

4. Conclusions and Outlook

In this study, we systematically investigated the geometrical and mechanical effects of varying environmental temperature and humidity during the FFF process, using a combination of analytical and experimental approaches. Regarding temperature, the temperature gradient within specimens was quantified, and the resulting warping defects were estimated and measured. The model and experiments show that increasing the environmental temperature from 30 °C to 90 °C could mitigate the warping defects by a 50 % reduction in curvature, as well as improve mechanical performance along the filament printing direction. Meanwhile, binding the specimen to the build plate is a worse choice (compared to increasing environmental temperature) since delamination may still happen.

Regarding humidity, the water absorption rate and saturation points of PC filaments were measured under different environmental humidity. The saturated filaments were then printed and characterized. While the water-generated porosity is less than estimated, it still showed a significant impact on the specimen's mechanical performance. Compared to printing with dried filaments, the specimens made of filaments with water content have inferior strength in both longitudinal (up to 30 % reduction) and transverse directions (up to 70 % reduction). However, compared to specimens with low water content (> 0 % by mass and < 0.10 % by mass), up to 50 % increase in ductility was observed in the transverse direction for higher water content (> 0.10 % by mass) specimens. This increase in ductility could be due to the combined effect of high porosity and non-uniform cross-section geometry: the crack propagates beyond the bond plane, and the long path in return gives more plastic dissipation. Overall, we recommend drying filaments before printing and to keep the printing environment dry and heated, especially for long jobs, for minimum geometric warping and good mechanical performance.

Besides practical recommendations to printer users, we envision our study opens new approaches to better estimate printing quality based on environmental conditions, which has been insufficiently studied before. Future research directions include both expanding to large scale samples and exploring other materials. For large scale samples, other parameters like raster angle, infill density, and the tool path will play important roles. Thus, the thermomechanical behaviors and the porosity-induced mechanical change will be more complex for prediction. For materials other than PC, different properties like crystallinity may need to be considered. To fully account for all those factors, a multi-physics multi-scale numerical model is needed in the future, considering multiple aspects

including solid mechanics, polymer dynamics, and molecular and chain dynamics. We hope our study could provide solid experimental foundations for such numerical studies.

Supplementary Materials: The following are available online at www.mdpi.com/xxx/s1, Figure S1: Uniaxial tension plot of Ultimaker filaments before and after printing; Table S1: Tabulated values of uniaxial tension specimens; Figure S2: Setup of the water absorption test; Figure S3: Calibration of PC's infrared emission; Figure S4: Measurements of strain within gauge area; Figure S5: Measurements of cross-section area with micro-CT; Figure S6: Measurements of PC's glass transition temperature; Figure S7: Measurements of PC's coefficient of thermal expansion.

Author Contributions: All authors have read and agree to the published version of the manuscript. Conceptualization, L.F. and S.H.K.; methodology, L.F., J.S. and S.H.K.; software, L.F.; validation, L.F., Y.Y. and O.A.; formal analysis, L.F. and Y.Y.; investigation, L.F., Y.Y., O.A., S.Y. and S.H.K.; resources, L.F and O.A.; data curation, L.F. and S.H.K.; writing—original draft preparation, L.F.; writing—review and editing, Y.Y., S.Y., O.A., J.S., and S.H.K.; visualization, L.F. and Y.Y.; supervision, S.H.K.; project administration, S.H.K.; funding acquisition, S.H.K.

Funding: This research was partially funded by National Science Foundation grant number DMREF-1628974, and the start-up fund from the Whiting School of Engineering at Johns Hopkins University.

Acknowledgments: We would like to thank Prof. Stavros Gaitanaros and Ms. Sirui Bi for allowing us to use their micro-CT machine, and Prof. Ryan Hurley and Dr. Chongpu Zhai for providing help on humidity control equipment. We also would like to thank Prof. Kevin J. Hemker, Prof. Thao D. Nguyen, Prof. Peter Olmsted, Prof. Mark O. Robbins, Dr. Jingkai Guo, Mr. Zheliang Wang and Mr. Marco Galvani Cunha for helpful comments and suggestions regarding this study. We appreciate STEGO, Inc. for donating the space heater.

Conflicts of Interest: The authors declare no conflict of interest. The funders had no role in the design of the study; in the collection, analyses, or interpretation of data; in the writing of the manuscript, or in the decision to publish the results.

References

(1) Lipson, H.; Kurman, M. *Fabricated: The New World of 3D Printing*; John Wiley & Sons, 2013.

(2) Ngo, T. D.; Kashani, A.; Imbalzano, G.; Nguyen, K. T. Q.; Hui, D. Additive Manufacturing (3D Printing): A Review of Materials, Methods, Applications and Challenges. *Composites Part B: Engineering* **2018**, *143*, 172–196. https://doi.org/10.1016/j.compositesb.2018.02.012.

(3) Dawoud, M.; Taha, I.; Ebeid, S. J. Mechanical Behaviour of ABS: An Experimental Study Using FDM and Injection Moulding Techniques. *Journal of Manufacturing Processes* **2016**, *21*, 39–45. https://doi.org/10.1016/j.jmapro.2015.11.002.

(4) Anitha, R.; Arunachalam, S.; Radhakrishnan, P. Critical Parameters Influencing the Quality of Prototypes in Fused Deposition Modelling. *Journal of Materials Processing Technology* **2001**, *118* (1), 385–388. https://doi.org/10.1016/S0924-0136(01)00980-3.

(5) Popescu, D.; Zapciu, A.; Amza, C.; Baciu, F.; Marinescu, R. FDM Process Parameters Influence over the Mechanical Properties of Polymer Specimens: A Review. *Polymer Testing* **2018**, *69*, 157–166. https://doi.org/10.1016/j.polymertesting.2018.05.020.

(6) Fang, L.; Yan, Y.; Agarwal, O.; Seppala, J. E.; Hemker, K. J.; Kang, S. H. Processing-Structure-Property Relationships of Bisphenol-A-Polycarbonate Samples Prepared by Fused Filament Fabrication. *Additive Manufacturing* **2020**, *35*, 101285. https://doi.org/10.1016/j.addma.2020.101285.

(7) Nidagundi, Vijay. B.; Keshavamurthy, R.; Prakash, C. P. S. Studies on Parametric Optimization for Fused Deposition Modelling Process. *Materials Today: Proceedings* **2015**, *2* (4), 1691–1699. https://doi.org/10.1016/j.matpr.2015.07.097.

(8) Montero, M.; Roundy, S.; Odell, D.; Ahn, S.-H.; Wright, P. K. Material Characterization of Fused Deposition Modeling (FDM) ABS by Designed Experiments. **2001**, 21.

(9) Wang, X.; Zhao, L.; Fuh, J. Y. H.; Lee, H. P. Effect of Porosity on Mechanical Properties of 3D Printed Polymers: Experiments and Micromechanical Modeling Based on X-Ray Computed Tomography Analysis. *Polymers* **2019**, *11* (7), 1154. https://doi.org/10.3390/polym11071154.

(10) Ahn, S.; Montero, M.; Odell, D.; Roundy, S.; Wright, P. K. Anisotropic Material Properties of Fused Deposition Modeling ABS. *Rapid Prototyping Journal* **2002**, *8* (4), 248–257. https://doi.org/10.1108/13552540210441166.

(11) Xia, H.; Lu, J.; Dabiri, S.; Tryggvason, G. Fully Resolved Numerical Simulations of Fused Deposition Modeling. Part I: Fluid Flow. *Rapid Prototyping Journal* **2018**, *24* (2), 463–476. https://doi.org/10.1108/RPJ-12-2016-0217.

(12) Yin, J.; Lu, C.; Fu, J.; Huang, Y.; Zheng, Y. Interfacial Bonding during Multi-Material Fused Deposition Modeling (FDM) Process Due to Inter-Molecular Diffusion. *Materials & Design* **2018**, *150*, 104–112. https://doi.org/10.1016/j.matdes.2018.04.029.

(13) Costa, S. F.; Duarte, F. M.; Covas, J. A. Thermal Conditions Affecting Heat Transfer in FDM/FFE: A Contribution towards the Numerical Modelling of the Process. *Virtual and Physical Prototyping* **2014**.

(14) Wang, T.-M.; Xi, J.-T.; Jin, Y. A Model Research for Prototype Warp Deformation in the FDM Process. *Int J Adv Manuf Technol* **2007**, *33* (11), 1087–1096. https://doi.org/10.1007/s00170-006-0556-9.

(15) Xinhua, L.; Shengpeng, L.; Zhou, L.; Xianhua, Z.; Xiaohu, C.; Zhongbin, W. An Investigation on Distortion of PLA Thin-Plate Part in the FDM Process. *Int J Adv Manuf Technol* **2015**, *79* (5), 1117–1126. https://doi.org/10.1007/s00170-015-6893-9.

(16) Xiaoyong, S.; Liangcheng, C.; Honglin, M.; Peng, G.; Zhanwei, B.; Cheng, L. Experimental Analysis of High Temperature PEEK Materials on 3D Printing Test. In *2017 9th International Conference on Measuring Technology and Mechatronics Automation (ICMTMA)*; IEEE: Changsha, China, 2017; pp 13–16. https://doi.org/10.1109/ICMTMA.2017.0012.

(17) Spoerk, M.; Arbeiter, F.; Raguž, I.; Weingrill, G.; Fischinger, T.; Traxler, G.; Schuschnigg, S.; Cardon, L.; Holzer, C. Polypropylene Filled With Glass Spheres in Extrusion-Based Additive Manufacturing: Effect of Filler Size and Printing Chamber Temperature. *Macromol. Mater. Eng.* **2018**, *303* (7), 1800179. https://doi.org/10.1002/mame.201800179.

(18) Martin, S.; Florian, A.; Ivan, R.; Gerhard, T.; Stephan, S.; Ludwig, C.; Clemens, H. The Consequences of Different Printing Chamber Temperatures in Extrusion-Based Additive Manufacturing. In *International Conference on Polymers and Moulds Innovations-PMI 2018*; Institute of Polymers and Composites, University of Minho, Portugal, 2018; p 6.

(19) Costa, A. E.; Ferreira da Silva, A.; Sousa Carneiro, O. A Study on Extruded Filament Bonding in Fused Filament Fabrication. *Rapid Prototyping Journal* **2019**, *25* (3), 555–565. https://doi.org/10.1108/RPJ-03-2018-0062.

(20) Armillotta, A.; Bellotti, M.; Cavallaro, M. Warpage of FDM Parts: Experimental Tests and Analytic Model. *Robotics and Computer-Integrated Manufacturing* **2018**, *50*, 140–152. https://doi.org/10.1016/j.rcim.2017.09.007.

(21) Mohamed, O. A.; Masood, S. H.; Bhowmik, J. L. Optimization of Fused Deposition Modeling Process Parameters: A Review of Current Research and Future Prospects. *Adv. Manuf.* **2015**, *3* (1), 42–53. https://doi.org/10.1007/s40436-014-0097-7.

(22) Bair, H. E.; Johnson, G. E.; Merriweather, R. Water Sorption of Polycarbonate and Its Effect on the Polymer's Dielectric Behavior. *Journal of Applied Physics* **1978**, *49* (10), 4976. https://doi.org/10.1063/1.324443.

(23) Qayyum, M. M.; White, J. R. Effect of Water Absorption and Temperature Gradients on Polycarbonate Injection Moldings. *Journal of Applied Polymer Science* **1991**, *43* (1), 129–144. https://doi.org/10.1002/app.1991.070430111.

(24) Ito, E.; Kobayashi, Y. Changes in Physical Properties of Polycarbonate by Absorbed Water. *Journal of Applied Polymer Science* **1978**, *22* (4), 1143–1149. https://doi.org/10.1002/app.1978.070220423.

(25) Narkis, M.; Nicolais, L.; Apicella, A.; Bell, J. P. Hot Water Aging of Polycarbonate. *Polymer Engineering & Science* **1984**, *24* (3), 211–217. https://doi.org/10.1002/pen.760240308.

(26) Li, C.; Zhang, Y.; Zhang, Y. Boiling Water Aging of Polycarbonate and Polycarbonate/Acrylonitrile–Butadiene–Styrene Resin and Polycarbonate/Low-Density Polyester Blends. *Journal of Applied Polymer Science* **2003**, *89* (3), 589–595. https://doi.org/10.1002/app.11825.

(27) Halidi, S. N. A. M.; Abdullah, J. Moisture Effects on the ABS Used for Fused Deposition Modeling Rapid Prototyping Machine. In *2012 IEEE Symposium on Humanities, Science and Engineering Research*; 2012; pp 839–843. https://doi.org/10.1109/SHUSER.2012.6268999.

(28) Kim, E.; Shin, Y.-J.; Ahn, S.-H. The Effects of Moisture and Temperature on the Mechanical Properties of Additive Manufacturing Components: Fused Deposition Modeling. *Rapid Prototyping Journal* **2016**, *22* (6), 887–894. https://doi.org/10.1108/RPJ-08-2015-0095.

(29) Valerga, A. P.; Batista, M.; Salguero, J.; Girot, F. Influence of PLA Filament Conditions on Characteristics of FDM Parts. *Materials* **2018**, *11* (8), 1322. https://doi.org/10.3390/ma11081322.

(30) Seppala, J. E.; Han, S. H.; Hillgartner, K. E.; Davis, C. S.; Migler, K. B. Weld Formation during Material Extrusion Additive Manufacturing. *Soft Matter* **2017**, *13* (38), 6761–6769. https://doi.org/10.1039/C7SM00950J.

(31) Klompen, E. T. J. Mechanical Properties of Solid Polymers : Constitutive Modelling of Long and Short Term Behaviour, Technische Universiteit Eindhoven, 2005.

(32) Wang C. M. Timoshenko Beam-Bending Solutions in Terms of Euler-Bernoulli Solutions. *Journal of Engineering Mechanics* **1995**, *121* (6), 763–765. https://doi.org/10.1061/(ASCE)0733-9399(1995)121:6(763).

(33) Lim, C. W.; Wang, C. M.; Kitipornchai, S. Timoshenko Curved Beam Bending Solutions in Terms of Euler-Bernoulli Solutions. *Arch. Appl. Mech.* **1997**, *67* (3), 179–190. https://doi.org/10.1007/s004190050110.

(34) Tsai, C.-L.; Lin, C.-C. Diffusion in a Solid Cylinder Part I: Advancing Model. *Journal of Marine Science and Technology* **2015**, *23* (2), 133–141. https://doi.org/10.6119/JMST-014-0117-1.

(35) J.D. Dymond; K.N. Marsh; R.C. Wilhoit. *Virial Coefficients of Pure Gases and Mixtures*; Springer, 2003.

(36) Peng, F.; Vogt, B. D.; Cakmak, M. Complex Flow and Temperature History during Melt Extrusion in Material Extrusion Additive Manufacturing. *Additive Manufacturing* **2018**, *22*, 197–206. https://doi.org/10.1016/j.addma.2018.05.015.

(37) Kusalik, P. G.; Liden, F.; Svishchev, I. M. Calculation of the Third Virial Coefficient for Water. *The Journal of Chemical Physics* **1995**, *103* (23), 10169–10175. https://doi.org/10.1063/1.469919.

(38) Harvey, A. H.; Lemmon, E. W. Correlation for the Second Virial Coefficient of Water. *Journal of Physical and Chemical Reference Data* **2004**, *33* (1), 369–376. https://doi.org/10.1063/1.1587731.

(39) Coogan, T. J.; Kazmer, D. O. Modeling of Interlayer Contact and Contact Pressure during Fused Filament Fabrication. *Journal of Rheology* **2019**, *63* (4), 655–672. https://doi.org/10.1122/1.5093033.

(40) Cox, D. R.; Oakes, D. *Analysis of Survival Data*; CRC Press, 1984.

(41) Gardner, R. J.; Martin, J. R. Humid Aging of Plastics: Effect of Molecular Weight on Mechanical Properties and Fracture Morphology of Polycarbonate. *Journal of Applied Polymer Science* **1979**, *24* (5), 1269–1280. https://doi.org/10.1002/app.1979.070240512.